Chemical and orbital fluctuations in $Ba_3CuSb_2O_9$

Yusuke Wakabayashi,[1,*] Daisuke Nakajima,[1] Yuki Ishiguro,[1] Kenta Kimura,[1] Tsuyoshi Kimura,[1] Satoshi Tsutsui,[2] Alfred Q. R. Baron,[2,3] Kouichi Hayashi,[4] Naohisa Happo,[5] Shinya Hosokawa,[6] Kenji Ohwada,[7] and Satoru Nakatsuji[8]

[1]*Division of Materials Physics, Graduate School of Engineering Science, Osaka University, Toyonaka 560-8531, Japan*

[2]*Japan Synchrotron Radiation Research Institute, SPring-8, Sayo, Hyogo 679-5198, Japan*

[3]*Materials Dynamics Laboratory, RIKEN SPring-8 Center, RIKEN, Sayo, Hyogo 679-5148, Japan*

[4]*Department of Materials Science and Engineering, Nagoya Institute of Technology, Gokiso-cho, Showa-ku, Nagoya, 466-8555, Japan*

[5]*School of Information Sciences, Hiroshima City University, Hiroshima 731-3194, Japan*

[6]*Department of Physics, Graduate School of Science and Technology, Kumamoto University, Kumamoto 860-8555, Japan*

[7]*Japan Atomic Energy Agency, Hyogo 679-5148, Japan*

[8]*Institute for Solid State Physics, The University of Tokyo, Kashiwa 277-8581, Japan*

(Received 11 November 2015; revised manuscript received 23 May 2016; published 7 June 2016)

Structural fluctuation in $Ba_3CuSb_2O_9$, which is proposed to exhibit a spin-orbital entangled state, has been studied by diffuse x-ray scattering, x-ray fluorescence holography, and inelastic x-ray scattering. Two kinds of spatial fluctuations are observed: temperature-independent and temperature-dependent ones. The former is related to Cu/Sb arrangement. The short-range chemical correlation in $Ba_3CuSb_2O_9$ is honeycomblike, whereas the correlation length is as short as the diameter of the honeycomb unit. The temperature variation of ferro- and antiferro-orbital correlations is extracted from Huang scattering intensity distributions. Both of these correlations increase with decreasing temperature down to 60 K, which corresponds to the energy of magnetic interaction of $Ba_3CuSb_2O_9$. A wide distribution of the characteristic time scale of the orbital motion is proposed from the spatial fluctuation of the ionic arrangement in $Ba_3CuSb_2O_9$.

DOI: 10.1103/PhysRevB.93.245117

I. INTRODUCTION

Spin and orbital degrees of freedom govern the physics of many transition metal oxides, and are known to be frustrated in certain geometrical structures [1–5]. While many (potentially) frustrated transition metal oxides have two degrees of freedom, they are usually decoupled because of the very different magnitudes of their interactions. Recently, it was proposed that $Ba_3CuSb_2O_9$ has a spin-orbital entangled state [6], providing us with an opportunity to study the possibility of this interesting quantum state.

The structure of $Ba_3CuSb_2O_9$ is studied in Ref. [6] by x-ray crystal structure and extended x-ray absorption fine structure (EXAFS) analyses. $Ba_3CuSb_2O_9$ is composed of Ba ions, SbO_6 octahedra and M_2O_9 bioctahedra as shown in Fig. 1. Because only Cu ions in $Ba_3CuSb_2O_9$ have spin and orbital degrees of freedom, the arrangement of the Cu ions defines the effective Hamiltonian. Based on the single-crystal x-ray structure analysis, each M site is occupied by 50% Cu and 50% Sb. Meanwhile, EXAFS measurements indicated each bioctahedron contains one Cu^{2+} and one Sb^{5+}. The two techniques give one answer: the crystal contains no Cu_2O_9 or Sb_2O_9 units but instead it contains $CuSbO_9$ units (inset of Fig. 1), and the orientation of the polarization vector $\boldsymbol{p}$ ($Cu^{2+} - Sb^{5+}$) has no long-range order. Diffuse x-ray scattering characterized by the wave vector (1/3,1/3,0) observed in x-ray photography has been assigned to the short-range arrangement of $\boldsymbol{p}$. Because the wave vector corresponds to the periodicity of a honeycomb structure, the local Cu arrangement is expected to be a honeycomb lattice.

The spin degree of freedom of $Ba_3CuSb_2O_9$ was found to be frustrated based on the magnetic properties described below [6]. Magnetic susceptibility measurements of $Ba_3CuSb_2O_9$ showed that the energy scale of the magnetic interaction is around 50 K. While some spins form spin singlets below 50 K, muon spin relaxation spectra indicate predominantly dynamic spin states down to 20 mK. Inelastic powder neutron scattering revealed that the low-temperature magnetic behavior appears to be gapless at 0.2-meV resolution. Therefore spins in $Ba_3CuSb_2O_9$ behave dynamically down to very low temperatures compared with the energy scale of the exchange interaction.

Following the experimental report (Ref. [6]), a number of theoretical and experimental studies have been conducted. A spin-orbital quantum liquid has been derived from the SU(4) symmetric Kugel-Khomskii Hamiltonian on the honeycomb lattice [7]. A spin-orbital resonant state associated with the dynamic Jahn-Teller (JT) effect is expected from a mean field calculation of the honeycomb cluster with certain values of parameters [8,9]. The spin-orbital resonant phase is located in the middle of the magnetically ordered phase and the orbital ordered phase in the parameter space. A first-principles band calculation [10] predicted a dynamic JT phase for the ferroic $\boldsymbol{p}$ structure, whereas the static JT phase is stabilized for the honeycomb arrangement of $\boldsymbol{p}$. Smerald and Mila [11] published a theoretical phase diagram for simple and decorated honeycomb lattices. They concluded that an emergent dimer phase, which involves nearest-neighbor spin singlets and orbital order, is the ground state for real $Ba_3CuSb_2O_9$ crystals, by noticing the complexity caused by the structural disorder.

Almost all theoretical work on $Ba_3CuSb_2O_9$ has focused on the honeycomb lattice or honeycomb cluster, even though the only experimental support for the honeycomb lattice is the broad peak around (1/3,1/3,0) in the x-ray photograph. The one exception [12] studies the short-range arrangement of $\boldsymbol{p}$ based on the Coulomb energy, and proposed that chemical disorder promotes the formation of a spin-orbital liquid state. As reported in Ref. [13], precise diffuse x-ray scattering measurements indicate that the peak position is considerably off from the commensurate (1/3,1/3,0) position, showing that the structure deviates from a regular honeycomb lattice.

*wakabayashi@mp.es.osaka-u.ac.jp

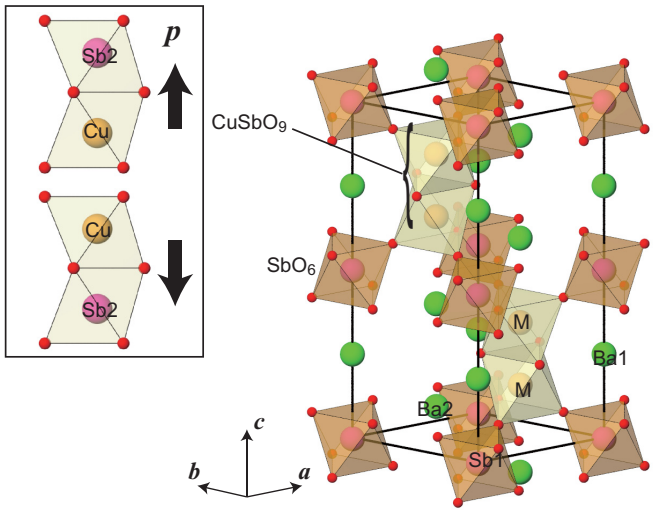

FIG. 1. Crystal structure of $Ba_3CuSb_2O_9$. Polarization vectors in $CuSbO_9$ units caused by the local arrangement of Cu^{2+} and Sb^{5+} have no long-range order within the crystal.

At this point, it is necessary to clarify two issues regarding $Ba_3CuSb_2O_9$: one is whether the JT distortion is dynamic, and the other is the local arrangement of Cu and Sb ions. These are not independent issues, because the latter can affect the magnetic and orbital interaction in $Ba_3CuSb_2O_9$ through lattice distortion.

Experimentally, it has been reported that some $Ba_3CuSb_2O_9$ crystals maintain a hexagonal lattice down to very low temperature, whereas others exhibit a hexagonal-to-orthorhombic transition around 200 K [6]. We refer to these types as hexagonal and orthorhombic samples, respectively. The difference is caused by the Cu/Sb stoichiometry of the crystals [13], while the microscopic origin of the difference is still unclear. The electron spin resonance (ESR) line shape of hexagonal samples is different from that of orthorhombic samples at low temperatures [13–15]. Very recently, it was reported that the JT effect in $Ba_3CuSb_2O_9$ is dynamic with a characteristic time scale of 10–100 ps based on the frequency dependence of its ESR signal [15].

In contrast to ESR and other magnetic measurements, x-ray scattering is a direct method to study JT distortion, which is strongly coupled with the orbital degree of freedom. Periodic arrangement of JT distortion is observed as Bragg peaks, and nonperiodic arrangement is observed as diffuse scattering around the Bragg peaks, which is called Huang scattering [16–18]. Using this method, we previously reported [19] that the growth of the ferro-orbital correlation in a hexagonal sample with decreasing temperature saturates around 60 K, which corresponds to the energy scale of the magnetic interaction. However, the temperature variation of the antiferro-orbital correlation was not studied. The characteristic time scale of orbital motion at low temperature is one of the central issues of the $Ba_3CuSb_2O_9$ system, but it has only been estimated from quasielastic scattering measurements at room temperature [19].

In this paper, we report chemical and orbital fluctuations in $Ba_3CuSb_2O_9$ measured over a wide temperature range. Experimental details are summarized in Sec. II. The short-range chemical correlation of Cu and Sb ions is studied by x-ray fluorescence holography (Sec. III A) and diffuse x-ray scattering (Secs. III B and III C). The analysis is reexamined in Sec. IV A. Temperature variation of the JT correlation, which depends strongly on the orbital correlation, is examined by measuring Huang scattering. Our analysis shows that not only the ferro-orbital correlation but also the antiferro-orbital correlation is developed with decreasing temperature down to 60 K. This result is reported in Sec. III D. The inelastic scattering spectra of Huang scattering intensity are presented in Sec. III E. Based on the structural fluctuation, the magnetic interaction (Sec. IV B) and orbital movement (Secs. IV C and IV D) of $Ba_3CuSb_2O_9$ are discussed.

II. EXPERIMENT

Single crystals of $Ba_3CuSb_2O_9$ used in the following experiments were grown by the flux method. The typical size of the crystals was 400 μm $\times$ 300 μm $\times$ 50 μm. X-ray fluorescence holography [20,21] measurements were performed at BL22XU of SPring-8, Japan. A single crystal of an orthorhombic sample was mounted on an Al rod with Apiezon grease. The beam size was limited to 300 μm(v) $\times$ 100 μm (h) to ensure that all of the incident beam hit the sample. The Cu $K\alpha$ fluorescent x rays were collected using an avalanche photodiode detector with a toroidal graphite energy analyzer. The measurements were performed by rotating two axes of the sample, $0^\circ \leqslant \theta \leqslant 65^\circ$ in steps of 1.0° and $0^\circ \leqslant \phi \leqslant 360^\circ$ in steps of $\sim 0.35^\circ$, where θ and ϕ are the incident angle and the azimuthal angle, respectively. Holograms were recorded at 16 different incident x-ray energies of 9.0–12.75 keV in steps of 0.25 keV. The average count rate of the Cu $K\alpha$ fluorescent x-rays was about 10^6 counts per second, and total exposure time was 48 hours. The holograms were symmetrized according to the crystal point symmetry $6/mmm$ before reconstructing the atomic images [22] to improve data statistics; for symmetrization, the crystal orientation was first examined by the x-ray diffraction, and adjusted to maximize the visibility of the x-ray standing wave lines seen in the hologram taken at 11 keV. Atomic images were reconstructed using Barton's method [23]. Since it has been pointed out that the matrix effect [24] or extinction effect [25] can cause artifact atomic images, we examined the effects on our reconstruction. The effects were found minor for our multiwavelength holograms; this is why we used simple Barton's method for our study. The spatial resolution of the current data is 0.5 Å (in-plane) and 0.6 Å (c direction).

Diffuse scattering away from the reciprocal lattice points was measured with a four-circle diffractometer attached to an 18-kW Mo rotating anode x-ray source. The incident x-ray was monochromatized by a bent graphite crystal. The signal was detected by a CdTe solid-state detector or NaI scintillation counter. Temperature variation of the diffuse intensity was measured with a hexagonal sample. The sample temperature was controlled with a closed-cycle refrigerator. The diffuse intensity in a large volume of the reciprocal space was measured at room temperature using an orthorhombic sample because the hexagonal crystal was smaller than the orthorhombic one, whereas their intensity distributions were basically the same [13], as shown later.

Diffuse scattering around the reciprocal lattice point was measured at BL-3A of the Photon Factory, KEK, Japan. This beamline has a four-circle diffractometer equipped with a closed-cycle refrigerator. An advantage of using synchrotron radiation is the high energy resolution, which results in little contamination of the diffuse intensity by the Bragg reflection. A hexagonal sample was used for this measurement to allow us to perform low-temperature measurements.

The inelastic x-ray scattering experiment was performed at BL35XU [26] of SPring-8, Japan. The incident x ray had an energy of 21.747 keV, and a Si (11 11 11) backscattering monochromator provided an energy resolution of 1.4 meV. The sample temperature was controlled with a closed-cycle refrigerator. A hexagonal crystal was used for this measurement.

Throughout this paper, we usually use hexagonal lattice parameters ($|\boldsymbol{a}| = |\boldsymbol{b}| = 5.81$ Å and $|\boldsymbol{c}| = 14.32$ Å) and the corresponding reciprocal lattice (hkl). We also use orthorhombic lattice parameters ($|\boldsymbol{a}_O| = |\boldsymbol{b}_O|/\sqrt{3} = 5.81$ Å and $|\boldsymbol{c}_O| = 14.32$ Å) and corresponding reciprocal lattice $(hkl)_O$ where noted.

III. RESULTS AND ANALYSIS

A. X-ray fluorescence holography

To clarify the local structure around Cu ions, an x-ray fluorescence holography measurement using the Cu K absorption edge was performed. This method observes the local structure around a selected element through the slight amount, typically 0.1%, of modulation in the angular dependence of the fluorescence intensity distribution caused by the interference. The intensity of the atomic image is proportional to the square of the atomic number and inversely proportional to the square of the distance from the Cu ion. The position of heavy elements within a few nanometers from the central atom is observed when the atomic positions relative to the central atom are well correlated [27]. Figure 2 shows some examples of the observed Cu K-edge holograms. The holograms are blurred when we compare them with the usual ones [21,22], suggesting that the Cu atoms in the present sample have a large fluctuation.

Figures 3(a)–3(d) show reconstructed atomic images on the c planes at distances of 0, 0.8, 1.4, and 2.3 Å, respectively, from a Cu ion, exhibiting the local structure around the Cu ion. These distances correspond to the Cu plane, Ba plane close to the Sb1 layer, the Ba plane at the center of $CuSbO_9$ bioctahedra, and the Sb1 plane, as depicted in Fig. 3(e). Using the reported results of the single-crystal structure analyses [13], one can predict the positions of atomic images for average structure. Solid and dashed circles in (a)–(d) indicate the expected atomic positions given by two different Cu positions connected by 6_3 spiral symmetry. We interpret the peaks inside the circles as atomic images, and those outside the circles as artifacts, which are sometimes observed in reconstructed images of disordered compounds.

The most important feature of this result is that only a few atoms are visible, which is a direct reflection of the blurred hologram images (Fig. 2). For example, Fig. 3(b) shows no Ba images inside the circles. This indicates that the atomic position of Cu has a large spatial fluctuation with respect to the surrounding lattice in the range of 5 Å to 5 nm from the Cu ion. In such a situation, (d) shows clear peaks for the nearest-neighbor Sb1 positions from the central Cu, while no atomic images are seen in the farther region. This result shows that there is detectable positional correlation between Cu and its nearest-neighbor Sb1. The intensity of atomic images of the nearest Sb1 sites shown in (d) is similar to that of the images of nearest-neighbor Ba in the nearest circles to the Cu ion in (c). In a well-correlated lattice, the Ba image is expected to be 1.8 times stronger than the Sb1 image because of its larger atomic number and closer proximity to the central Cu ion. Therefore the positional correlation between Cu-Sb1 correlation is stronger than that of the Cu-Ba. The present x-ray fluorescence holography analysis showed there is rigid short-range order around the Cu ion by reconstructing neighbor Sb1 and Ba atoms, and that the Cu-Sb1 correlation is the strongest, while the Cu-Ba correlation is weaker.

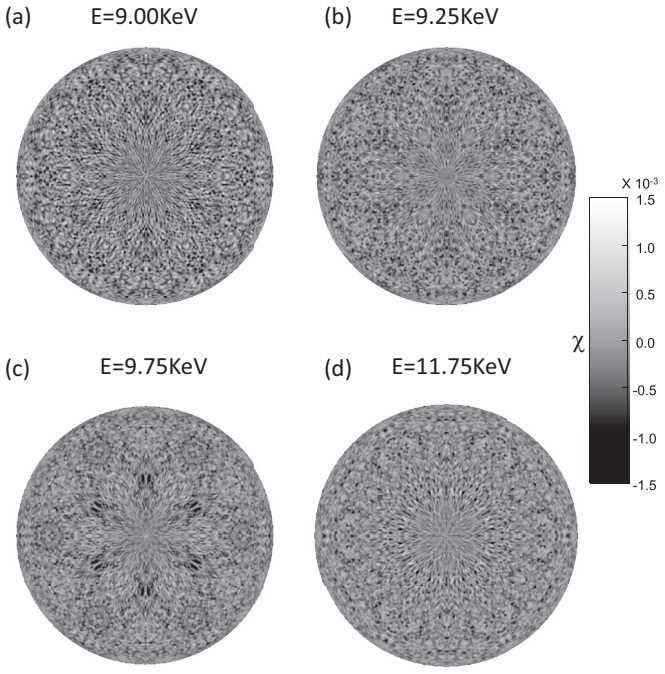

FIG. 2. Hologram images taken with the incident x ray of (a) 9.00, (b) 9.25, (c) 9.75, and (d) 11.75 keV. Radial and angular coordinates show the incident angle θ (0° to 65°) and azimuthal angle ϕ (0° to 180°) of the x-ray fluorescence holography measurements.

B. Features of diffuse x-ray scattering

Other than the thermal fluctuation, which causes the thermal diffuse scattering, there are two kinds of structural fluctuations in $Ba_3CuSb_2O_9$. One of them is orbital fluctuation, which can be observed through Huang scattering. The orbital fluctuation can be dynamic, and is known to depend on temperature [19]. The other is chemical fluctuation, which can be expressed by the spatial arrangement of $\boldsymbol{p}$, and is totally static in nature. We call the diffuse x-ray scattering caused by the former orbital diffuse scattering, and that by the latter chemical diffuse scattering.

Diffuse x-ray scattering intensity distribution maps around $(\frac{5}{2}\frac{5}{2}2)$ [$= (502)_O$] and $(\frac{5}{2}\frac{5}{2}3)$ [$= (503)_O$] of orthorhombic and hexagonal samples are presented in Fig. 4. The maps are basically the same for the two samples. In accordance with our previous report [13], the diffuse intensity clearly shows internal structure within a Brillouin zone. The intensity maxima are obviously deviated from the $(\frac{1}{3}\frac{1}{3}0)$ position, especially in the $l = 3$ plane.

The temperature dependence of diffuse intensity around $(3.4,0,2)_O$, which is classified as scattering away from the reciprocal lattice position, was measured for a hexagonal sample. The result is presented in Fig. 5. In contrast to the temperature dependent Huang scattering caused by JT distortion [19], the intensity around $(3.4,0,2)_O$ is independent of temperature, suggesting that it is chemical diffuse scattering.

To clarify the chemical short-range order structure of $Ba_3CuSb_2O_9$, we measured the diffuse intensity in a large volume in reciprocal space. The diffuse intensity distribution

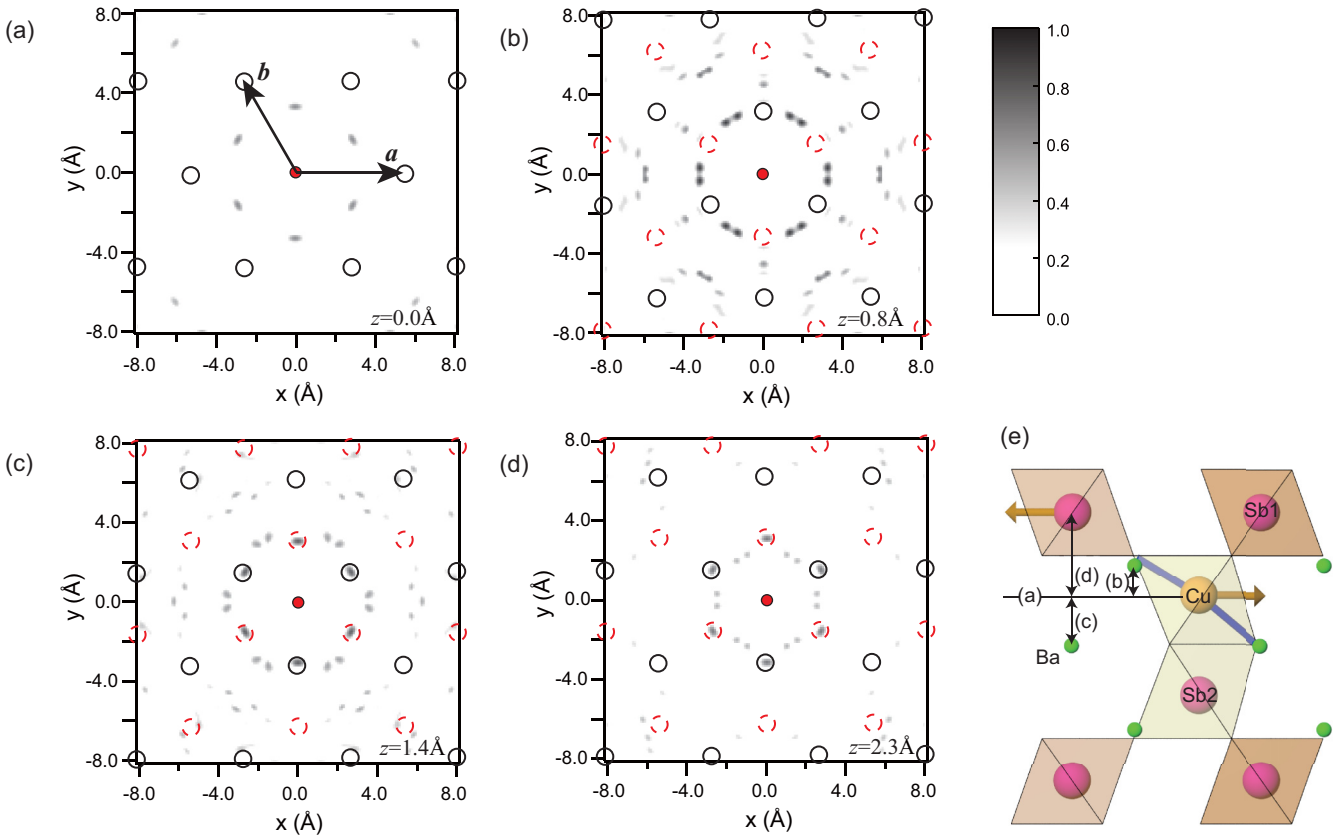

FIG. 3. Atomic images on the c-planes located at distances from a Cu ion of (a) 0, (b) 0.8, (c) 1.4, and (d) 2.3 Å. The Cu ion is shown as a (red) circle at the center of each panel. Solid and dashed circles show the expected atomic positions given by two different Cu positions connected by 6_3 spiral symmetry [for (a), the dashed circles overlap to solid ones]. (e) Resulting local structure model. In this figure, $\boldsymbol{p}$ points downward, and the JT distortion of CuO_6 makes the Cu-O bond shown as a thick (blue) line longer. This JT distortion pushes the upper left SbO_6 away, and the reaction pushes the CuO_6 in the opposite direction. These atomic displacements of Sb and Cu are represented as (yellow) arrows.

within an $(\xi 0 \zeta)_O$ plane is presented in Fig. 6. Background intensity caused by air scattering was subtracted. Intensity maxima are only seen on integer l lines. This means that the correlation along the c direction is ferroic [28]. Some examples of $(\xi \eta l)$ maps are provided in Fig. 7. The $l = 0$ plane has no diffuse intensity away from the reciprocal lattice positions (open circles), while the $l = 3$ plane has some intensity away from the Bragg positions. The diffuse intensity distribution contains peaks, forming arcs around the reciprocal lattice points $(n, n + 3m, 3)$, where n and m are integers. The diffuse intensity away from the Bragg position is very weak on the $l = 4$ plane, as illustrated in (c), i.e., the intensity oscillates with varying l. This means the origin of the diffuse intensity has a spatial correlation involving the c direction.

There are three types of diffuse scattering, i.e., thermal, orbital and chemical diffuse scattering. While the first two are observed around the Bragg points, the intensity distribution of the last one is unknown. To make clear the chemical short-range structure, we need to know if the chemical diffuse scattering contributes to the intensity around the Bragg reflections. Figures 7(a)–7(c) reveal intensity maxima for the diffuse scattering away from the Bragg position, which corresponds to the chemical diffuse scattering, within an a^*-b^* plane are similar to each other. Only l affects the maxima. This implies that only a limited number of ions, probably one or two heavy atoms in the minimum structural unit, are involved in the scattering. In contrast, thermal diffuse scattering and Huang scattering intensity are concentrated around reciprocal lattice points, and proportional to the intensity of the central Bragg reflection, which varies considerably. Therefore one can determine the origin of diffuse scattering centered at a Bragg position by comparing its intensity with that of the central Bragg reflection. Figure 7(d) presents a magnified view of the intensity map around weak Bragg reflections 122, 112, and 212. If the chemical diffuse scattering appears at the reciprocal lattice points, those Bragg reflections also have some diffuse intensity having width and intensity similar to those of the chemical diffuse peaks away from the Bragg peaks. Apparently, there is no such intensity around them. Therefore we conclude that the chemical diffuse scattering in this compound appears only away from the Bragg positions.

C. Diffuse x-ray scattering originating from chemical disorder

Each $CuSbO_9$ bioctahedron can be expressed by the polarization vector $\boldsymbol{p}$ as shown in the inset of Fig. 1, and $\boldsymbol{p}$ have no long-range order in their directions (up and down). In the present case, the arrangement of $\boldsymbol{p}$ is a triangular Ising lattice. The effective interaction between $\boldsymbol{p}$ should be antiferroic because of the absence of pyroelectricity [6]. The arrangement of the polarization vectors shows the Ising spin arrangement just below the melting temperature at which the crystal was

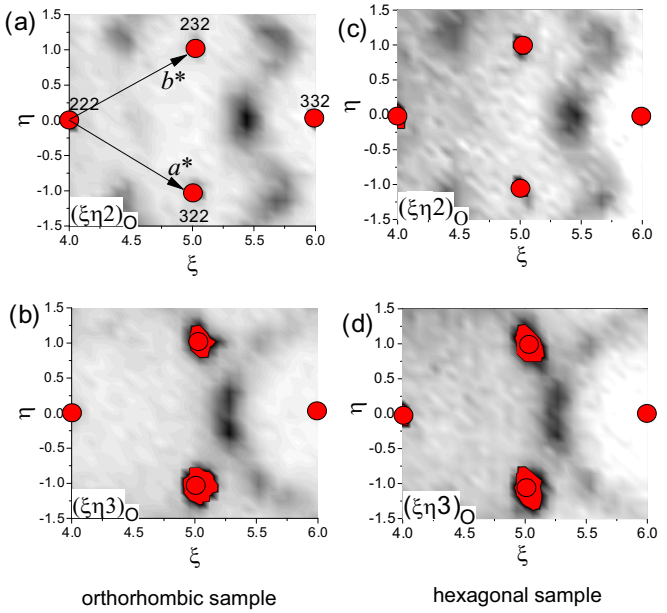

FIG. 4. Diffuse scattering intensity distribution maps around $(502)_O$ and $(503)_O$ for [(a) and (b)] orthorhombic and [(c) and (d)] hexagonal samples. The measurements were performed at room temperature. Reciprocal lattice points are indicated by (red) circles. Indices of a hexagonal lattice are seen in (a).

originally grown. In the case of an Ising arrangement, the deviation of the electron density of each $CuSbO_9$ unit from the average structure has a negative correlation with the c plane [29], which leads to no scattering intensity on the $l = 0$ plane. This is what we observed in Fig. 7(a).

To obtain the pair distribution function (PDF) of $\boldsymbol{p}$, we performed Fourier transformation of the chemical diffuse scattering [30–33]. The intensity data were measured in the triangular areas $(0,0,l)_O$–$(5.8,0,l)_O$–$(5.8,5.8,l)_O$ (typical maps are presented in Fig. 7), and the maps were expanded by the symmetry operation. All integer values of $|l|$ up to 8 were taken into account. To extract the chemical diffuse

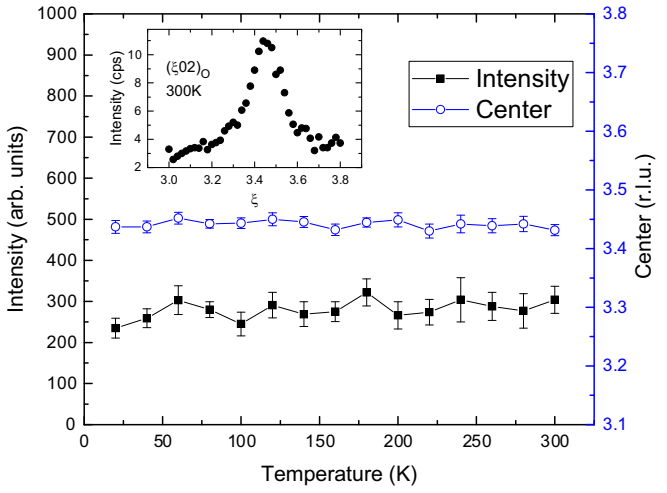

FIG. 5. Temperature variation of the intensity (closed squares) and peak position (open circles) of the diffuse intensity around $(3.4402)_O$.

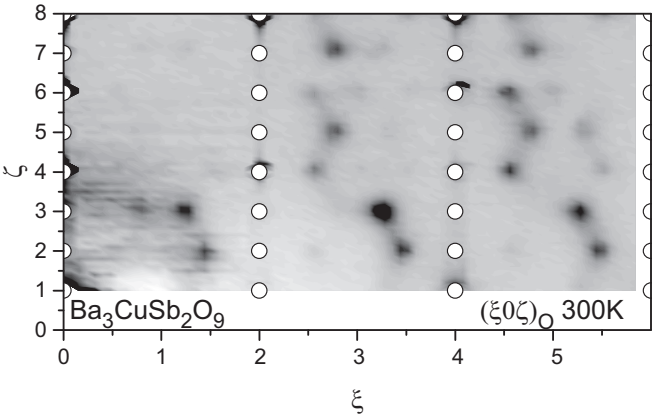

FIG. 6. Diffuse intensity map on the h_O-l plane. Open circles show the reciprocal lattice points.

scattering, we eliminated the intensity within the area of $(h \pm 0.16, k \pm 0.32, l)_O$ ($h + k$: even) because the intensity close to the Bragg position mainly consists of the Huang scattering and thermal diffuse scattering. This procedure is essential to obtain the chemical correlation, because the thermal diffuse scattering and Huang scattering involve all the atoms in a unit cell, resulting the PDF corresponding to the total average crystal structure. Similar data treatment is sometimes made for the analysis of diffuse scattering [31,33–35].

Figure 8(a) shows the PDF on the c plane. The large positive peak at the origin is the correlation with itself. The height at the origin is sensitive to the estimated background level, and thus has no quantitative information. The negative correlation at $\boldsymbol{a}$ means antiferroic coupling with the neighboring polarization vector (Cu^{2+} to Sb^{5+}) $\boldsymbol{p}$. There are also positive correlation peaks at $\boldsymbol{a} + 2\boldsymbol{b}$ and equivalent positions. The intensity of the positive peak is the same as that of the negative one. We also found some peaks as high as 1/4 of the above-mentioned ones at $2\boldsymbol{a}$ (negative), $2\boldsymbol{a} + 4\boldsymbol{b}$ (negative), and $4\boldsymbol{a}$ (positive) positions. Because these correlations are rather weak and hard to distinguish from artifacts, we neglected these weak features in the later analysis.

To reproduce the in-plane correlation, we constructed seven-membered cluster models. Figure 8(b) shows two examples of the PDF. The left-hand side of panel (b) shows the PDF for the honeycomb cluster shown in the corresponding inset, which is expected from the previous report [6]. The discrepancy from panel (a) is apparent. The right-hand side of panel (b) shows the model that reproduces the PDF with the best of the seven-membered cluster models considered. This model has peaks with intensities of $-2/7$ at $\boldsymbol{a}$, $2/7$ at $2\boldsymbol{a} + \boldsymbol{b}$, and $-1/7$ at $2\boldsymbol{a}$. The first two features successfully reproduce the experimentally obtained PDF. The last one, $-1/7$ at $2\boldsymbol{a}$, is also observed in panel (a) with a weak intensity. Therefore the short-range Cu/Sb arrangement is well explained with this cluster. Because the structure of this cluster is part of a honeycomb lattice, we call it a "honeycomb-like correlation."

To visualize the real-space arrangement of Cu and Sb ions, we performed a Monte Carlo calculation using the software DISCUS [36]. The calculation was made to reproduce the correlation $-C$ at $\boldsymbol{a}$, $+C$ at $\boldsymbol{a} + 2\boldsymbol{b}$, zero at $2\boldsymbol{a}$ and $3\boldsymbol{a}$ for a $50 \times 50 \times 1$ structure with $C = 0.28 \sim 2/7$. The obtained real-space arrangement of Cu and Sb ions is presented in Fig. 8(c). The difference in the symbol size represents the different types of elements. This calculation successfully

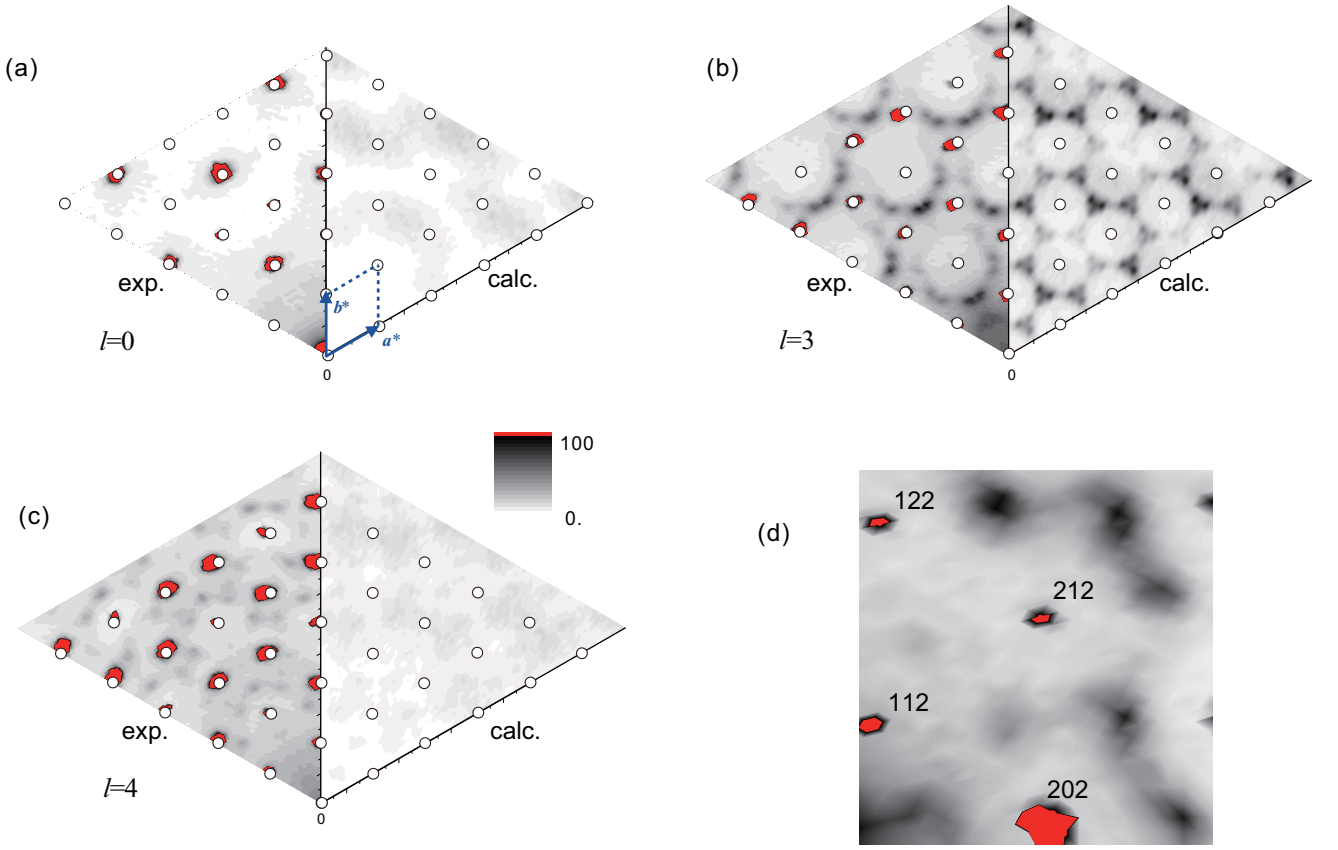

FIG. 7. Diffuse scattering intensity distribution maps at the (a) $l = 0$, (b) $l = 3$, and (c) $l = 4$ planes. The left half of each panel shows the experimental results, and the right half of each panel shows the calculated intensity distribution with $C = 0.28$ (see text). The measurements were performed for the triangular areas $(0,0,l)_O$–$(5.8,0,l)_O$–$(5.8,5.8,l)_O$, and the maps were expanded by the symmetry operation. Reciprocal lattice positions in the hexagonal coordinate are marked by open circles. (d) Magnified view of the intensity map around the 212 Bragg reflection.

reproduces the peaks in the intensity distribution within a Brillouin zone. However, we still failed to reproduce the asymmetric diffuse intensity distribution with respect to the reciprocal lattice points. This feature reflects the local structure within the unit cell.

Using the atomic image obtained from the holography measurement (Fig. 3) as well as previously reported results from single-crystal structure analysis [13] and EXAFS [6], we constructed a final model for the structure of $Ba_3CuSb_2O_9$. According to our holography measurement, the size of the well-correlated structure unit is presented in Fig. 3(e). The corner-shared $Sb1O_6$ octahedron is pushed away from the Cu ion by JT distortion, and the reaction pushes the Cu ion away from the $Sb1O_6$ octahedron. The magnitude of the Cu and Sb1 displacements was fixed to 0.1 Å, which was determined from the JT distortion obtained by EXAFS analysis. The orientation of the JT distortion was chosen at random for each site. Such a local structure unit was embedded to the Cu/Sb arrangement shown in Fig. 8(c). The calculated diffuse intensity distribution maps are presented in Fig. 7, together with the experimental results. The dependence of the overall intensity on l and the arc-shaped intensity distribution are well reproduced in the calculation. Therefore our x-ray experiments support the above-mentioned short-range chemical structure of $Ba_3CuSb_2O_9$. Figure 9(a) shows the diffuse intensity distribution on the $l = 3$ plane calculated for $C = 0$, 0.1, 0.2, and 0.28 together with the experimental result. The experimental result appears to be reproduced when the value of C is around 0.1 to 0.2. The left and right panels of (b) depict the real space Cu/Sb arrangement for $C = 0.1$ and 0.2, respectively. The validity of the structure model will be discussed in Sec. IV A.

D. Diffuse x-ray scattering originating from orbital arrangement

As we reported earlier [19], the orbital degree of freedom of Cu ions causes a strain field through JT distortion, and this strain field produces diffuse x-ray scattering around reciprocal lattice positions, known as Huang scattering. Huang scattering reflects the Fourier transform of the strain field. Breathing mode distortion gives rise to the diffuse intensity spread from Bragg peaks along the radial direction in the reciprocal space. JT mode distortion induces the diffuse scattering spread to the perpendicular direction as shown in Fig. 10 (see Appendix for details).

Figure 10(a) shows the temperature variation of the Huang intensity around the 220 Bragg reflection of $Ba_3CuSb_2O_9$; the results for 4 and 290 K are already reported in Ref. [19], while others are firstly reported here. The intensity increased as the temperature decreased. In addition, the intensity distribution at low temperature was more anisotropic than that at high

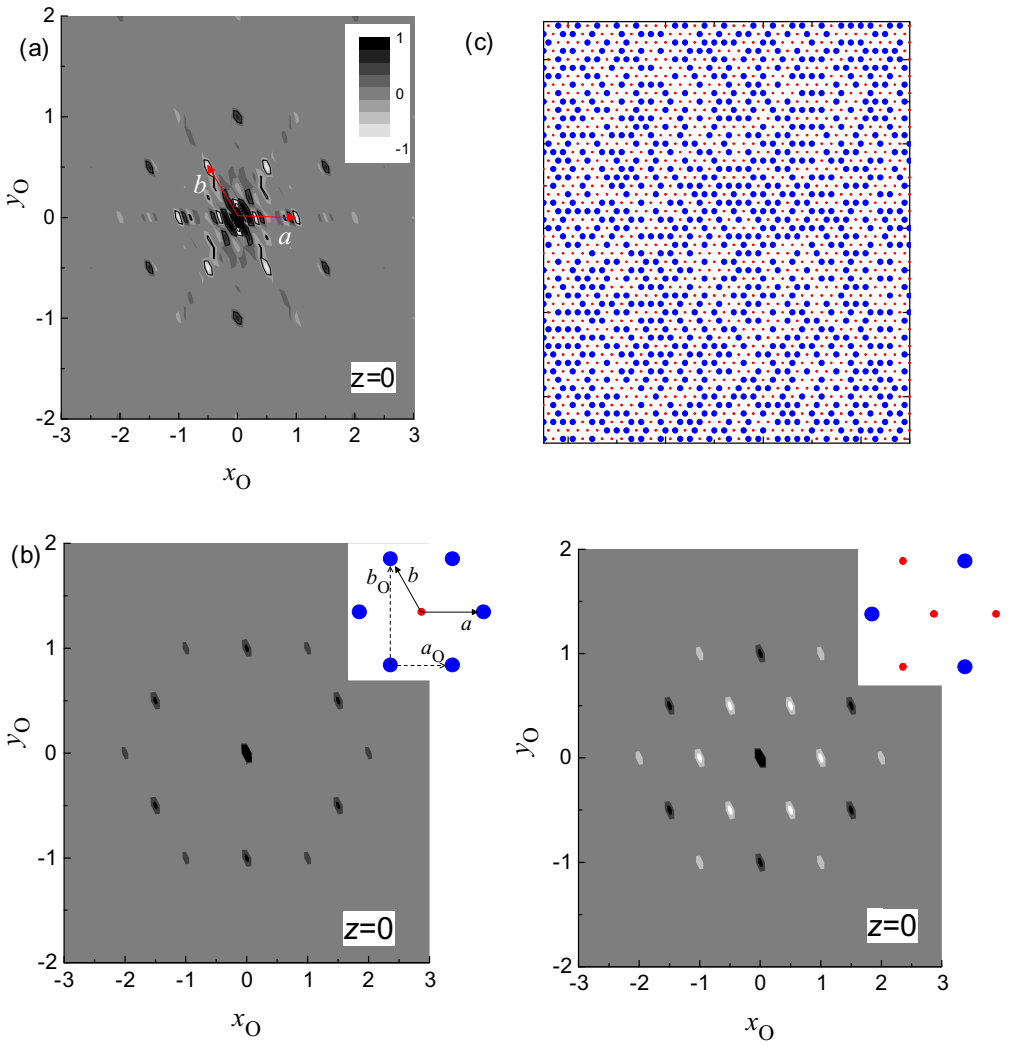

FIG. 8. (a) Pair distribution function (PDF) within the $z = 0$ plane based on experimental results. (b) Two examples of PDFs of the seven-membered cluster models shown in the insets. The difference in the size of the symbols in the insets represents the different types of elements (Cu or Sb). The length scales of the figures are the same as those in (a). (c) Real-space arrangement of Cu and Sb obtained through a Monte Carlo calculation based on the PDF $-C$ at $\boldsymbol{a}$, $+C$ at $\boldsymbol{a} + 2\boldsymbol{b}$, zero at $2\boldsymbol{a}$ and $3\boldsymbol{a}$ with $C = 0.28 \sim 2/7$.

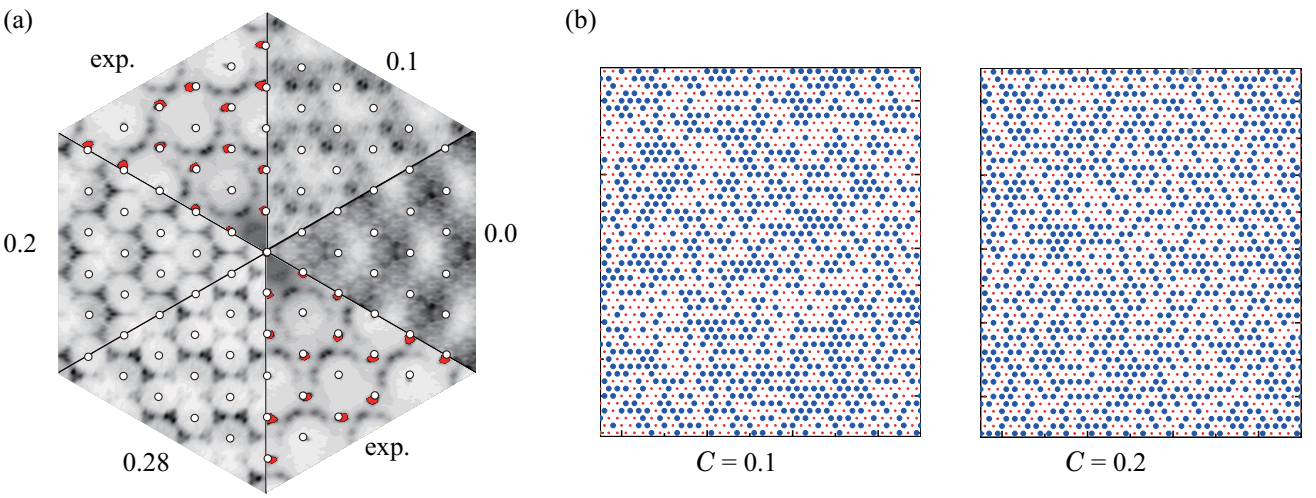

FIG. 9. (a) Calculated diffuse intensity map on the $l = 3$ plane for $C = 0$, 0.1, 0.2, and 0.28, together with experimental results. The color scale for each calculation has been adjusted to aid visualization. (b) Real-space Cu/Sb distribution maps for $C = 0.1$ and 0.2.

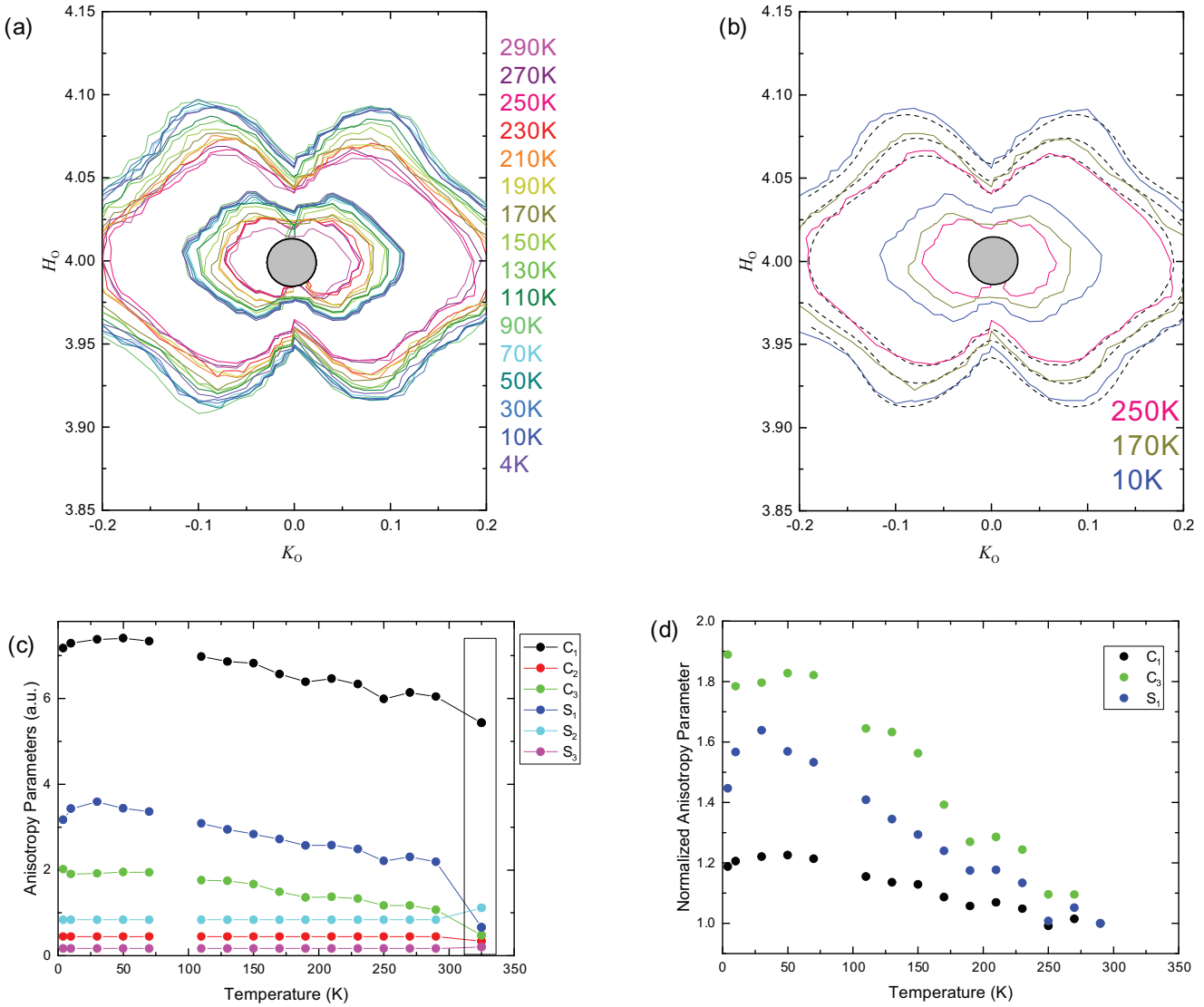

FIG. 10. (a) Huang scattering intensity distribution around the 220 [$= (400)_O$] Bragg reflection measured at various temperatures. The contour lines for 10^3 and 10^4 counts per second are shown. (b) Huang scattering intensity distributions for selected temperatures. Dashed curves show the reproduced contours based on Eq. (2). (c) Temperature variation of the anisotropy of Huang intensity. The parameters in the box (325 K) shows the values for an isolated JT distortion field. (d) Anisotropy parameters normalized by those at 290 K as a function of temperature.

temperature. This temperature variation is caused by the development of a short-range orbital correlation [19].

Assuming that the whole JT-induced strain field is represented by the sum of the lattice distortion caused by each orbital in the crystal, the diffuse intensity $I_{\rm diff}$ at the scattering vector $\boldsymbol{Q}$ is written as

$$I_{\rm diff}(\boldsymbol{Q}) = N \sum_{\alpha,\beta=1}^{3} \left[\sum_{m} \langle \rho^{\alpha}(\boldsymbol{0}) \rho^{\beta}(\boldsymbol{r}_m) \rangle \exp(i\,\boldsymbol{Q}\cdot\boldsymbol{r}_m) \right] \times \boldsymbol{Q}\cdot\boldsymbol{t}^{\alpha *}(\boldsymbol{q})\ \boldsymbol{Q}\cdot\boldsymbol{t}^{\beta}(\boldsymbol{q}), \quad (1)$$

where $\rho^{\alpha}(\boldsymbol{r}_m)$ denotes the occupancy of orbital α of the mth site at position $\boldsymbol{r}_m$, $\boldsymbol{t}^{\alpha}(\boldsymbol{q})$ is the Fourier transform of the strain induced by orbital α at the origin with $\boldsymbol{q}$ the deviation of $\boldsymbol{Q}$ from the reciprocal lattice point nearby, and N is the number of orbitals in the sample (see Appendix for derivation). The sum over m is taken over the whole crystal, and provides the Fourier transform of the PDF of the orbitals $\langle \rho^{\alpha}(\boldsymbol{0}) \rho^{\beta}(\boldsymbol{r}) \rangle$. The asterisk denotes the complex conjugate.

According to the reported EXAFS measurement [6], the shape of the CuO_6 octahedra is temperature independent. Thus, one can expect that the strain field around a CuO_6 octahedron $\boldsymbol{t}$ is also temperature independent. Because there are only two variables, $\langle \rho^{\alpha}(\boldsymbol{0}) \rho^{\beta}(\boldsymbol{r}_m) \rangle$ and $\boldsymbol{t}^{\alpha}(\boldsymbol{q})$, the temperature variation of the Huang diffuse intensity reflects that of $\langle \rho^{\alpha}(\boldsymbol{0}) \rho^{\beta}(\boldsymbol{r}_m) \rangle$. In our previous report, we only analyzed the ferro-orbital ordering correlation as a function of temperature [19]. This is simply because the ferro-orbital ordering component is easy to extract from the intensity distribution. The degree of the antiferro-orbital ordering correlation is observed as the anisotropy of the Huang intensity distribution. To quantify this anisotropy, we reproduced the contour line for 1000 counts per second in Fig. 10(a) using the following formula with a polar coordinate

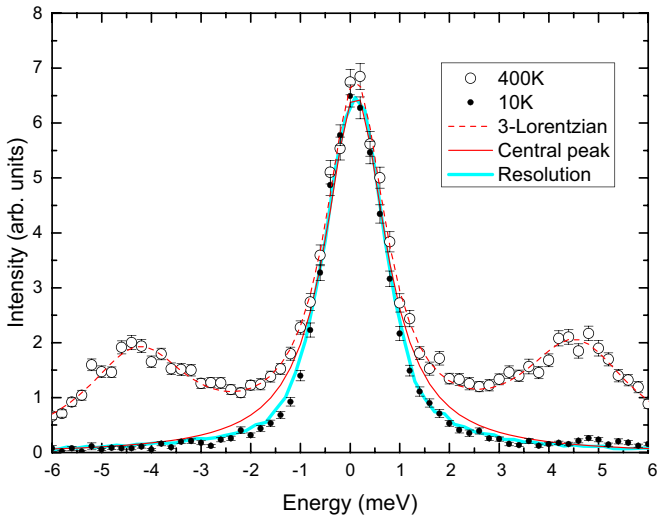

FIG. 11. Quasielastic scattering spectra measured at (3.8 4.2 0) at 400 K (open symbols) and 10 K (closed symbols) normalized at zero energy transfer. The peaks at ±4.5 meV seen in the 400-K plots correspond to acoustic-mode phonons. Three-Lorentzian fitting was used to extract the central peak for 400-K data. The resolution profile is also presented.

around the Bragg position:

$$C(\theta) = \sum_n \left[C_n \cos^2(n\theta) + S_n \sin^2(n\theta)\right], \qquad (2)$$

where θ is the phase angle from the horizontal axis, $C(\theta)$ denotes the distance of the contour line from the Bragg position, and C_n and S_n are fitting parameters. The summation was taken up to $n = 3$. The dashed curves in Fig. 10(b) are the typical results of the fitting. The outer contour curves were successfully reproduced by the formula. The anisotropy parameters are plotted in panel (c). The parameters for an isolated JT distortion field are also shown in the box. We found that the parameters C_2, S_2, and S_3 are small and temperature independent, thus we fixed them to the corresponding values at 290 K. Only three parameters, C_1, C_3, and S_1, are needed to reproduce the anisotropy of Huang intensity. The largest parameter, C_1, best describes the Huang scattering from noncorrelated and ferroically correlated orbitals. The parameter S_1 corresponds to the intensity along the H_O axis, while Huang scattering from isolated JT distortion has much smaller S_1 value. This may be caused by the interaction between JT distorted octahedra. Therefore the parameter C_3 is the best measure of the antiferro-orbital correlation in the investigated system. The parameters normalized by the values at 290 K are provided in panel (d). The physical aspects of this temperature variation will be discussed in Sec. IV C.

E. Quasielastic x-ray scattering on the meV scale

To study the characteristic time of the JT motion in $Ba_3CuSb_2O_9$, we measured quasielastic x-ray scattering spectra of the Huang scattering at (3.8 4.2 0) at 400 and 10 K. The peak width is proportional to the inverse of the lifetime of lattice distortion [19,37,38]. Note that strong JT coupling induces a strong correlation between orbital and lattice distortion. The results are shown in Fig. 11 together with the instrumental resolution. The energy resolution was determined using the scattering from polymethyl methacrylate. The full width at half-maximum (FWHM) of the resolution profile estimated by the Lorentzian fitting is 1.32(2) meV.

The 400-K profile has three peaks; the two side peaks around ± 4.5 meV correspond to acoustic-mode phonons. To separate the quasielastic component, three-Lorentzian fitting was employed. The dashed curve shows the result of the fitting, and the thin solid curve shows the extracted quasielastic component for 400 K data. The quasielastic component looks slightly broader than the resolution, with a FWHM of 1.47(2) meV. The 0.15(4) meV broadening may be caused by the short lifetime of orbital motion. Another possible origin is multiphonon scattering, i.e., two or more phonons whose total momentum is (−0.2 0.2 0) are created/annihilated in the scattering process. Such a scattering process sometimes gives a broad peak around zero-energy transfer [39].

In contrast, the 10-K data plots fall on the resolution curve. The FWHM was 1.25(2) meV, which gives an intrinsic width of −0.07(4) meV. The small negative width means that this profile is as sharp as the resolution within the experimental accuracy. This indicates the orbital motion is much slower than the instrumental resolution (∼3 ps), at least at low temperature.

IV. DISCUSSION

A. Re-examination of short-range order

In Sec. III C, we started from the Cu-Sb correlation as the origin of the chemical diffuse scattering, while the final structure model shows that the diffuse intensity is mainly caused by the atomic displacement. We re-examine our results in this section.

The minimum unit of the structure model is the $CuSbO_9$ bioctahedron. This unit has six variants; i.e., two directions of $\boldsymbol{p}$ and three directions of JT distortion. Our final structural model consists of a random distribution of three JT directions with a correlated arrangement of $\boldsymbol{p}$. In principle, the spatial correlation of the JT direction observed in Sec. III D affects the diffuse intensity distribution, which was not taken into account in our model. To estimate the effect of JT direction on the chemical diffuse scattering intensity, we made another model, which is called the ferro-orbital model. This model has the same Cu/Sb arrangement as that in Fig. 8(c), but all CuO_6 octahedra have the same JT direction. We calculated the scattering intensity for the three directions of ferro arrangements, and averaged them to take into account the multidomain structure. The degree of ferro-orbital arrangement is so high that the crystal spontaneously distorts into the orthorhombic phase. Therefore this calculation shows the exaggerated effect of ferro-orbital arrangement. The intensity change induced by the ferro-orbital arrangement from Fig. 7(b) was less than twice. Therefore the effect of the correlation in the JT direction on the diffuse intensity distribution is minor. This is consistent with the temperature variation of the chemical diffuse scattering shown in Fig. 5 and that of the Huang scattering illustrated in Fig. 10(d). The latter clearly shows finite temperature variation of the JT direction, while the former shows no temperature variation. As a result, it is reasonable to obtain the spatial arrangement of $\boldsymbol{p}$ from the diffuse intensity away from the Bragg positions and determine the orbital arrangement from the Huang scattering distribution.

Now we are prepared to explain the discrepancy between the real space reconstruction of holography [Fig. 3(a)] and PDF obtained from the chemical diffuse scattering [Fig. 8(a)]. While the two images show the same spatial region, only the latter shows a clear correlation. The reason for this discrepancy is the difference of the value observed by the two methods. As

we discussed above, the chemical diffuse scattering mainly observes the chemical correlation of Cu/Sb. In contrast, x-ray fluorescence holography is more sensitive to the positional correlation. We performed holographic reconstruction on $C = 0.1$ arrangement [Fig. 9(b)] with- and without the horizontal [Fig. 3(e)] and vertical [13] atomic displacements (not shown). As expected, the 0.1 Å of Cu and Sb1 displacements, which induce the chemical diffuse scattering, make the atomic images at $\boldsymbol{a}$ as weak as 1/3.

There are minor discrepancies between the observed and calculated diffuse maps shown in Fig. 7. For example, the calculated intensity for the $l = 4$ plane is too weak, or the peaks in the $l = 3$ plane look like doublets in the experimental result but triplets in the calculated map. The former is caused by the simplified local structure. The long-wavelength undulation in reciprocal space is caused by the structure in a narrow region in real space. Because our structural model consists of only Cu and Sb1, slight displacement of other atoms can provide such modulation. As for the latter, the discrepancy is found in a narrow region in reciprocal space, and is caused by the wide-range structure in real space. One possibility is that the weak $2\boldsymbol{a}$, $2\boldsymbol{a} + 4\boldsymbol{b}$ and $4\boldsymbol{a}$ correlations we neglected in the Monte Carlo calculation are the source of this discrepancy. Although there are such minor discrepancies, we succeeded in reproducing the main features of the chemical diffuse scattering using an extremely simple model, displaced Cu-Sb1 pairs arranged with negative and positive correlation at $\boldsymbol{a}$ and $\boldsymbol{a} + 2\boldsymbol{b}$ positions.

The obtained Cu/Sb arrangement presented in Fig. 8(c) is very similar to the theoretically determined structure reported by Smerald and Mila [12]. Their calculation indicated a stable arrangement of $\boldsymbol{p}$ in the Ising triangular lattice at the crystal growth temperature, while our structure is derived from experimental observations at room temperature. The similarity between the results is remarkable because the two procedures are very different.

B. Effect of spatial fluctuation on magnetic interaction

Our x-ray measurements reveal spatial fluctuation of the atomic arrangement in $Ba_3CuSb_2O_9$ at room temperature. We estimate the effect of this fluctuation on its magnetic interactions. The main magnetic interaction paths are shown in Fig. 12(a) as $J1$, $J1'$, and $J2$ [6]. For each path, the d-d process, which involves a spin exchange between the Cu and $M1$ or $M2$ site through two oxygens, and the d-p-d process, which involves double occupancy on an oxygen site, are dominant [8]; these processes are schematically illustrated in (b) and (c), respectively. The intensity of the superexchange interaction for the d-d process is proportional to $t_{dp1}^2 t_{pp}^2 t_{dp2}^2 \cos^2\alpha \cos^2\beta$, and that for the d-p-d process is proportional to $t_{dp1}^2 t_{pp}^2 t_{dp2}^2 (\cos^2\alpha \sin^2\beta + \cos^2\beta \sin^2\alpha)$, where t_{dp1}, t_{dp2}, and t_{pp} denote the transfer integrals between Cu-O, M-O, and O-O, respectively, and α and β are Cu-O-O and M-O-O angles, respectively. Based on our local structure model, the fluctuation in exchange interaction caused by that of the bond angle is as large as 3% of the total exchange interaction. If we use the bond-length (l) dependence of the d-p transfer integral [40] $l^{-3.5}$, the fluctuation of exchange interaction is ∼20%. If we assume a static d orbital, the exchange interaction has a large anisotropy. The dp transfer integral between $3z^2 - r^2$ and z orbitals presented in Fig. 12(b) is twice as large as that between $3x^2 - r^2$ and z in the same atomic arrangement, so the fluctuation of the superexchange interaction is therefore 16-fold.

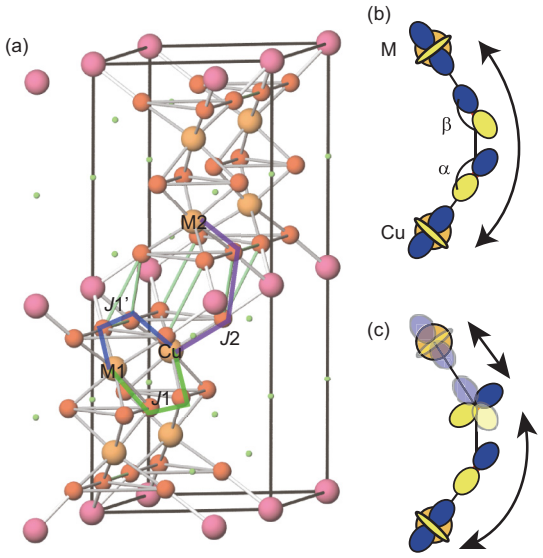

FIG. 12. Major exchange paths from Cu to the $M1$ site ($J1$ and $J1'$) and Cu to the $M2$ site ($J2$).

C. Temperature variation of orbital fluctuation

There are two types of crystals, i.e., the orthorhombic sample and the hexagonal sample. Despite the two samples have different ground states, we found no distinct difference in the average structure [13] as well as chemical fluctuation; only the difference is 0.05% of expansion in the a lattice parameter. Since the hexagonal-orthorhombic phase transition is a ferro-orbital phase transition, we examine the temperature variation of the orbital fluctuation in the hexagonal sample. As we mentioned in Sec. III D, the spatial correlation of orbitals is expressed by the parameters C_1, C_3, and S_1. The parameter C_1 shows similar temperature variation to the ferro-orbital correlation described in our previous report [19], in which the ferro-orbital correlation was estimated in a very different way. The coincidence of this variation indicates the reliability of our analyses. The parameter C_3, which reflects the antiferro-orbital correlation, increases monotonically with decreasing temperature down to 60 K, which is the characteristic temperature for magnetism. Other than 60 K, there is no characteristic temperature for antiferro-orbital correlation. Both ferro- and antiferro-orbital fluctuations increase with decreasing temperature in the hexagonal sample. In the case of the orthorhombic sample, the ferro-orbital fluctuation overwhelms the antiferro-orbital fluctuation around 200 K. The difference between the hexagonal and orthorhombic samples is caused by the competitive fluctuation of ferro- and antiferro-orbital correlations.

Temperature variation of the short-range orbital arrangement has been observed experimentally. Shanavas *et al.* [10] suggested that the orbital arrangement is static in a honeycomb structure because of the anisotropic potential caused by the chemical Cu-Sb arrangement. If the chemical arrangement makes the orbital static, the orbital arrangement cannot be altered by temperature variation below room temperature. It should be noted, however, that they also suggested that JT distortion is dynamic in a triangular lattice structure, in which Cu-Sb2 polarization vectors ($\boldsymbol{p}$) align ferroically.

Our measurements reveal the arrangement of $\boldsymbol{p}$ is neither honeycomb nor ferroic, but fluctuates spatially. Several ferroic clusters are found in Figs. 8(c) and 9(b). In light of the short-range ordered structure of $\boldsymbol{p}$, their theoretical work suggests an almost continuous distribution of the binding energy of JT distortion in the fluctuated lattice.

Another possible situation is the spin-orbital liquid state caused by the delocalized orphan spins [12]. Because the simulated structure factor in Ref. [12] resembles our experimental one, their prediction appears plausible.

D. Time scale of orbital fluctuation

Our inelastic x-ray scattering measurements show that the lifetime of the JT distortion field is basically static at low temperature, and the broadening of the quasielastic signal is tiny even at 400 K. Here, we examine the inelastic spectra taking into account spatial fluctuation. Let us assume that the binding energy of the direction of JT distortion is continuously distributed as discussed above. In such a situation, some of the orbitals are frozen from very high temperature, and others remain dynamic down to low temperatures. In the inelastic scattering experiments, the static component provides a sharp energy spectrum, while the dynamic component gives a broad energy spectrum, and is thus harder to detect. Therefore the wide distribution of the binding energy makes the inelastic scattering more sensitive to the static component than the dynamic component.

Time scale of the orbital fluctuation can also be estimated from the range of the strain field caused by the JT distortion. The Huang scattering intensity increases monotonically as the magnitude of $\boldsymbol{q}$ decreases down to 0.04 $\boldsymbol{b}_O^*$; this value is resolution limited. This result suggests the length scale of the strain field is larger than $b_O/0.04 \sim 15$ nm. If we assume that this size is defined by the sound velocity multiplied by the JT time scale, we obtain the JT time scale of slower than 2 ps. Here, we used the sound velocity of the longitudinal acoustic phonon, 6.8 km/s derived from the inelastic x-ray scattering [19]. This time scale is consistent with the recent report on ESR measurements [15].

V. CONCLUSION

We performed diffuse x-ray scattering, x-ray fluorescence holography, and inelastic x-ray scattering measurements to clarify chemical and orbital correlations in $Ba_3CuSb_2O_9$. The PDF of Cu/Sb chemical short-range arrangement was found to be honeycomblike. The resultant Cu/Sb arrangement is in good agreement with a theoretically derived stable arrangement [12]. The JT distortion of CuO_6 octahedra induces characteristic local distortion [see Fig. 3(e)]. The effect of this local distortion on the exchange interaction was discussed. Orbital correlation was studied through JT distortion. Both ferro- and antiferro-orbital correlations develop with decreasing temperature down to 60 K, which corresponds to the energy of magnetic interaction. This means both types of orbital correlations are affected by magnetism. Based on the inelastic x-ray scattering spectra, the temporal fluctuation of the JT distortion at 10 K appears to be static for the time resolution of ~3 ps. This time scale is consistent with recently reported ESR measurements [15]. In addition, the spatial fluctuation induces large diversity in the potential barriers of the three JT directions, which results in a wide range of the characteristic time scale of orbital fluctuation.

ACKNOWLEDGMENTS

The authors thank H. Sawa, N. Katayama, M. Hagiwara, S. Ishihara, and J. Nasu for valuable discussions. This work was supported by Grants-in-Aid for Scientific Research (JSPS KAKENHI, Grants No. 26287080, No. 26105006, and No. 26105008). The synchrotron radiation experiments at the Photon Factory and SPring-8 were performed with the approval of the (Photon Factory Program Advisory Committee (Proposals No. 2012G091 and No. 2014S2-003) and the (Japan Synchrotron Radiation Research Institute (JASRI) (Proposals No. 2013A1240 and No. 2014A3783), respectively.

APPENDIX: HUANG SCATTERING FROM CORRELATED POLARONS

Here, we derive Eq. (1). Scattering amplitude $F(\boldsymbol{Q})$ from a distorted lattice is written as

$$\begin{aligned} F(\boldsymbol{Q}) &= \sum_k \exp[i\,\boldsymbol{Q}\cdot\{\boldsymbol{R}_k + \boldsymbol{t}(\boldsymbol{R}_k)\}] \\ &\simeq \sum_k \exp[i\,\boldsymbol{Q}\cdot\boldsymbol{R}_k][1 + i\,\boldsymbol{Q}\cdot\boldsymbol{t}(\boldsymbol{R}_k)] \\ &= \sum_k \exp[i\,\boldsymbol{Q}\cdot\boldsymbol{R}_k] + i\,\boldsymbol{Q}\cdot\sum_k \boldsymbol{t}(\boldsymbol{R}_k)\exp[i\,\boldsymbol{Q}\cdot\boldsymbol{R}_k], \end{aligned} \tag{A1}$$

where $\boldsymbol{R}_k$ and $\boldsymbol{t}(\boldsymbol{R}_k)$ denote the average position and small displacement of the kth atom, respectively. The atomic form factor is omitted for simplicity. The first summation gives the Bragg reflection, and the second summation gives the diffuse scattering amplitude $F_{\rm diff}(\boldsymbol{Q})$. The diffuse term can be written as $i\,\boldsymbol{Q}\cdot\boldsymbol{t}(\boldsymbol{q})$, where $\boldsymbol{t}(\boldsymbol{q})$ is the Fourier transform of the distortion field. When the distortion field is originated from isolated point defects, such as distorted MO_6 octahedron in oxides, the scattering is called Huang scattering. The diffuse intensity is proportional to $|\boldsymbol{Q}\cdot\boldsymbol{t}(\boldsymbol{q})|^2$. Intensity distributions caused by the JT distortion and breathing mode distortion around the 220 Bragg reflection of a hexagonal lattice (400 in the orthorhombic setting) are presented in Fig. 13.

Next, we apply this general formula to our specific case. Let $\boldsymbol{t}^\alpha(\boldsymbol{r})$ be the distortion field caused by the orbital $\alpha(=1,2,3)$ at the origin. The total distortion $\boldsymbol{T}(\boldsymbol{r}_k)$ is approximated as the

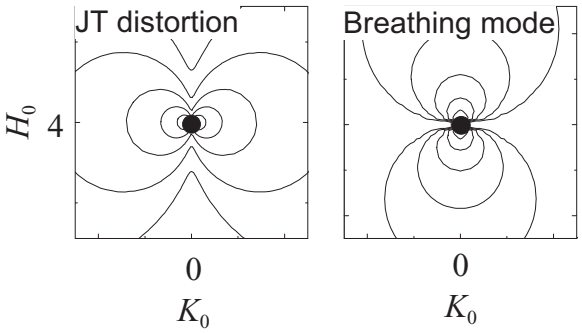

FIG. 13. Huang scattering intensity distribution caused by (left) JT distortion and (right) breathing mode distortion. Elastic constants used for the calculation are the values of $Ba_3CuSb_2O_9$ reported in Ref. [19]. The calculation for the JT distortion case took into account the sixfold symmetry of the crystal.

sum of each orbital.

$$\boldsymbol{T}(\boldsymbol{r}_k) = \sum_j \sum_\alpha \rho^\alpha(\boldsymbol{r}_j)\boldsymbol{t}^\alpha(\boldsymbol{r}_k - \boldsymbol{r}_j), \tag{A2}$$

where $\rho^\alpha(\boldsymbol{r}_j)$ is 1 when the jth site is occupied by orbital α, and zero otherwise. Using this expression, $F_{\rm diff}(\boldsymbol{Q})$ is

$$\begin{aligned} F_{\rm diff}(\boldsymbol{Q}) &= i\,\boldsymbol{Q}\cdot\sum_k \boldsymbol{T}(\boldsymbol{r}_k)\exp[i\,\boldsymbol{Q}\cdot\boldsymbol{r}_k] \\ &= i\,\boldsymbol{Q}\cdot\sum_{kj\alpha}\rho^\alpha(\boldsymbol{r}_j)\boldsymbol{t}^\alpha(\boldsymbol{r}_k-\boldsymbol{r}_j) \\ &\quad\times\exp[i\,\boldsymbol{Q}\cdot(\boldsymbol{r}_k-\boldsymbol{r}_j)]\exp[i\,\boldsymbol{Q}\cdot\boldsymbol{r}_j] \\ &\equiv i\,\boldsymbol{Q}\cdot\sum_\alpha \rho^\alpha(\boldsymbol{Q})\boldsymbol{t}^\alpha(\boldsymbol{q}). \end{aligned} \tag{A3}$$

The diffuse intensity $I_{\rm diff}(\boldsymbol{Q})$ is

$$\begin{aligned} &F^*_{\rm diff}(\boldsymbol{Q})F_{\rm diff}(\boldsymbol{Q}) \\ &= -i\,\boldsymbol{Q}\cdot\sum_{km\alpha}\rho^\alpha(\boldsymbol{r}_m)\boldsymbol{t}^\alpha(\boldsymbol{r}_k-\boldsymbol{r}_m)\exp[-i\,\boldsymbol{Q}\cdot\boldsymbol{r}_k] \\ &\quad\times i\,\boldsymbol{Q}\cdot\sum_{ln\beta}\rho^\beta(\boldsymbol{r}_n)\boldsymbol{t}^\beta(\boldsymbol{r}_l-\boldsymbol{r}_n)\exp[i\,\boldsymbol{Q}\cdot\boldsymbol{r}_l] \\ &= \sum_{klmn\alpha\beta}\rho^\alpha(\boldsymbol{r}_m)\rho^\beta(\boldsymbol{r}_n)\,\boldsymbol{Q}\cdot\boldsymbol{t}^\alpha(\boldsymbol{r}_k-\boldsymbol{r}_m)\,\boldsymbol{Q}\cdot\boldsymbol{t}^\beta(\boldsymbol{r}_l-\boldsymbol{r}_n) \\ &\quad\times\exp[i\,\boldsymbol{Q}\cdot(\boldsymbol{r}_l-\boldsymbol{r}_k)]. \end{aligned} \tag{A4}$$

Substituting $\boldsymbol{r}_k$ for $\boldsymbol{r}_k-\boldsymbol{r}_m$ and $\boldsymbol{r}_l$ for $\boldsymbol{r}_l-\boldsymbol{r}_n$, one obtains

$$\begin{aligned} &= \sum_{klmn\alpha\beta}\rho^\alpha(\boldsymbol{r}_m)\rho^\beta(\boldsymbol{r}_n)\,\boldsymbol{Q}\cdot\boldsymbol{t}^\alpha(\boldsymbol{r}_k)\,\boldsymbol{Q}\cdot\boldsymbol{t}^\beta(\boldsymbol{r}_l) \\ &\quad\times\exp[i\,\boldsymbol{Q}\cdot(\boldsymbol{r}_l+\boldsymbol{r}_n-\boldsymbol{r}_k-\boldsymbol{r}_m)] \\ &= \sum_{mn\alpha\beta}\rho^\alpha(\boldsymbol{r}_m)\rho^\beta(\boldsymbol{r}_n)\exp[i\,\boldsymbol{Q}\cdot(\boldsymbol{r}_n-\boldsymbol{r}_m)]\,\boldsymbol{Q}\cdot\boldsymbol{t}^{\alpha*}(\boldsymbol{q})\,\boldsymbol{Q}\cdot\boldsymbol{t}^\beta(\boldsymbol{q}) \\ &= \sum_{n\alpha\beta}N\langle\rho^\alpha(0)\rho^\beta(\boldsymbol{r}_n)\rangle\exp[i\,\boldsymbol{Q}\cdot(\boldsymbol{r}_n)]\,\boldsymbol{Q}\cdot\boldsymbol{t}^{\alpha*}(\boldsymbol{q})\,\boldsymbol{Q}\cdot\boldsymbol{t}^\beta(\boldsymbol{q}). \end{aligned} \tag{A5}$$

Now we obtain Eq. (1).

[1] L. Balents, Nature (London) **464**, 199 (2010).
[2] S. Ishihara, M. Yamanaka, and N. Nagaosa, Phys. Rev. B **56**, 686 (1997).
[3] G. Khaliullin and S. Maekawa, Phys. Rev. Lett. **85**, 3950 (2000).
[4] B. Keimer, D. Casa, A. Ivanov, J. W. Lynn, M. v. Zimmermann, J. P. Hill, D. Gibbs, Y. Taguchi, and Y. Tokura, Phys. Rev. Lett. **85**, 3946 (2000).
[5] D. I. Khomskii and M. V. Mostovoy, J. Phys. A: Math. Gen. **36**, 9197 (2003).
[6] S. Nakatsuji, K. Kuga, K. Kimura, R. Satake, N. Katayama, E. Nishibori, H. Sawa, R. Ishii, M. Hagiwara, F. Bridges, T. U. Ito, W. Higemoto, Y. Karaki, M. Halim, A. A. Nugroho, J. A. Rodriguez-Rivera, M. A. Green, and C. Broholm, Science **336**, 559 (2012).
[7] P. Corboz, M. Lajkó, A. M. Läuchli, K. Penc, and F. Mila, Phys. Rev. X **2**, 041013 (2012).
[8] J. Nasu and S. Ishihara, Phys. Rev. B **88**, 094408 (2013).
[9] J. Nasu and S. Ishihara, Phys. Rev. B **91**, 045117 (2015).
[10] K. V. Shanavas, Z. S. Popovic, and S. Satpathy, Phys. Rev. B **89**, 085130 (2014).
[11] A. Smerald and F. Mila, Phys. Rev. B **90**, 094422 (2014).
[12] A. Smerald and F. Mila, Phys. Rev. Lett. **115**, 147202 (2015).
[13] N. Katayama, K. Kimura, Y. Han, J. Nasu, N. Drichko, Y. Nakanishi, M. Halim, Y. Ishiguro, R. Satake, E. Nishibori, M. Yoshizawa, T. Nakano, Y. Nozue, Y. Wakabayashi, S. Ishihara, M. Hagiwara, H. Sawa, and S. Nakatsuji, Proc. Natl. Acad. Sci. USA **112**, 9305 (2015).
[14] S.-H. Do, J. van Tol, H. D. Zhou, and K.-Y. Choi, Phys. Rev. B **90**, 104426 (2014).
[15] Y. Han, M. Hagiwara, T. Nakano, Y. Nozue, K. Kimura, M. Halim, and S. Nakatsuji, Phys. Rev. B **92**, 180410(R) (2015).
[16] P. H. Dederichs, J. Phys. F: Met. Phys. **3**, 471 (1973).
[17] S. Shimomura, N. Wakabayashi, H. Kuwahara, and Y. Tokura, Phys. Rev. Lett. **83**, 4389 (1999).
[18] L. Vasiliu-Doloc, S. Rosenkranz, R. Osborn, S. K. Sinha, J. W. Lynn, J. Mesot, O. H. Seeck, G. Preosti, A. J. Fedro, and J. F. Mitchell, Phys. Rev. Lett. **83**, 4393 (1999).
[19] Y. Ishiguro, K. Kimura, S. Nakatsuji, S. Tsutsui, A. Q. R. Baron, T. Kimura, and Y. Wakabayashi, Nat. Commun. **4**, 2022 (2013).
[20] M. Tegze and G. Faigel, Nature (London) **380**, 49 (1996).
[21] K. Hayashi, N. Happo, S. Hosokawa, W. Hu, and T. Matsushita, J. Phys.: Condens. Matter **24**, 093201 (2012).
[22] M. Tegze, G. Faigel, S. Marchesini, M. Belakhovsky, and A. I. Chumakov, Phys. Rev. Lett. **82**, 4847 (1999).
[23] J. J. Barton, Phys. Rev. Lett. **67**, 3106 (1991).
[24] D. T. Dul, K. M. Dabrowski, and P. Korecki, Europhys. Lett. **104**, 66001 (2013).
[25] P. Korecki, D. V. Novikov, M. Tolkiehn, and G. Materlik, Phys. Rev. B **69**, 184103 (2004).
[26] A. Q. R. Baron, Y. Tanaka, S. Goto, K. Takeshita, T. Matsushita, and T. Ishikawa, J. Phys. Chem. Solids **61**, 461 (2000).
[27] K. Hayashi, N. Happo, and S. Hosokawa, J. Electron Spectrosc. Relat. Phenom. **195**, 337 (2014).
[28] If the polarization arrangement along the c direction has antiferro coupling, the short-range ordering exhibits $2c$ periodicity that provides diffuse scattering characterized by the wave vector of $\frac{1}{2}c^*$. The experimental result shows all the signals centered at integer-l planes, indicating that the short-range arrangement of $\boldsymbol{p}$ is ferroic.
[29] Let the electron densities for $\boldsymbol{p}$ parallel and antiparallel to $\boldsymbol{c}$ be $\rho_\uparrow(\boldsymbol{r})$ and $\rho_\downarrow(\boldsymbol{r})$. They are transformed into each other by a mirror operation with respect to the c plane. The deviation of $\rho_\uparrow(\boldsymbol{r})$ from the average $[\Delta\rho(\boldsymbol{r})]$ is $[\rho_\uparrow(\boldsymbol{r})-\rho_\downarrow(\boldsymbol{r})]/2$. As a result, $\Delta\rho(\boldsymbol{r})$ has a negative correlation with the c plane.
[30] B. E. Warren, *X-ray Diffraction* (Dover, New York, 1969), Sec. 12.4.
[31] Y. Wakabayashi, N. Wakabayashi, M. Yamashita, T. Manabe, and N. Matsushita, J. Phys. Soc. Jpn. **68**, 3948 (1999).
[32] T. Weber and A. Simonov, Z. Kristallogr. **227**, 238 (2012).

[33] A. Simonov, T. Weber, and W. Steurer, J. Appl. Cryst. **47**, 2011 (2014).

[34] Y. Wakabayashi, A. Kobayashi, H. Sawa, H. Ohsumi, N. Ikeda, and H. Kitagawa, J. Am. Chem. Soc. **128**, 6676 (2006).

[35] M. Kobas, T. Weber, and W. Steurer, Phys. Rev. B **71**, 224205 (2005).

[36] R. B. Neder and T. Proffen, *Diffuse Scattering and Defect Structure Simulations: A Cook Book Using the Program* DISCUS (Oxford Science Publications, UK, 2008).

[37] K. Kakurai, T. Sakaguchi, M. Nishi, C. M. E. Zeyen, S. Kashida, and Y. Yamada, Phys. Rev. B **53**, R5974 (1996).

[38] D. N. Argyriou, J. W. Lynn, R. Osborn, B. Campbell, J. F. Mitchell, U. Ruett, H. N. Bordallo, A. Wildes, and C. D. Ling, Phys. Rev. Lett. **89**, 036401 (2002).

[39] A. Q. R. Baron, H. Uchiyama, R. Heid, K. P. Bohnen, Y. Tanaka, S. Tsutsui, D. Ishikawa, S. Lee, and S. Tajima, Phys. Rev. B **75**, 020505(R) (2007).

[40] W. A. Harrison, *Electronic Structure and the Properties of Solids* (Dover, New York, 1989).